1-1-2007

Emergence of Singular Structures in Oldroyd-B Fluids

Becca Thomases
Courant Institute of Mathematical Sciences, bthomases@smith.edu

Michael Shelley
Courant Institute of Mathematical Sciences

Emergence of Singular Structures in Oldroyd-B Fluids

Becca Thomases[1], and Michael Shelley[1]

[1]Courant Institute of Mathematical Sciences, New York University
New York City, NY 10012

Abstract. Numerical simulations reveal the formation of singular structures in the "polymer" stress field of a viscoelastic fluid modelled by the Oldroyd-B equations. These singularities emerge exponentially in time at hyperbolic points in the flow and their algebraic structure depends critically on the Weissenberg number. Beyond a critical Weissenberg number the stress field approaches a cusp-singularity and beyond a second critical Weissenberg number the stress becomes unbounded exponentially in time. A local approximation to the solution at the hyperbolic point is constructed and there is excellent agreement between the local solution and the simulations. Although the stress field becomes unbounded for sufficiently large Weissenberg number, the resultant forces of stress remain bounded. Artificially enforcing finite polymer chain lengths via a FENE-P penalization appears to keep the stress bounded, but a cusp-singularity is still approached exponentially in time.

1 Introduction

Recent experimental work [1, 2, 3, 4] on the mixing of viscoelastic fluids at low Reynolds number has led us to consider the Oldroyd-B model for viscoelastic fluids in the zero Reynolds number limit for a standard curvilinear flow. We report on results for mixing in [5], but while investigating this phenomena we have observed the formation of singular structures in dynamical solutions of the Oldroyd-B equations, which we report on here. Oldroyd-B is a popular continuum model of a so-called "Boger" fluid, having a simple and elegant structure but also some well documented flaws; see for example [6]. The Oldroyd-B equations can be derived from microscopic principles by assuming a linear Hooke's law for the restoring force under distension of the immersed polymer coils; see [7]. The Oldroyd-B model is often criticized for this simplification because the linear Hooke's law puts no restriction on the length of polymer chains. Related to this, in an extensional rheological flow the steady Oldroyd-B equations can exhibit stress divergences [8]. Here we consider low Reynolds number flow with biperiodic boundary conditions using the Stokes-Oldroyd-B equations. This allows us to use a spectral method to evolve the system which is helpful to deduce the analytic structure of the flow and monitor the numerical accuracy of solutions. The geometry of the flow is set up with a time independent background force, which in the pure Newtonian case yields the four roll mill. In the full nonlinear system the polymer stress acts as an additional force which drives the evolution of the fluid velocity.

The four roll mill geometry of the flow creates a central hyperbolic stagnation point. We find the emergence, exponentially in time, of nearly singular structures in the stresses at every Weissenberg number. These singular structures appear as "stress islands" in the diagonal components of the stress tensor which lie along the unstable manifold associated with the hyperbolic point. The regularity of the singular structures decreases as the Weissenberg number increases. For sufficiently small Weissenbreg number, these singularities are high-order. There are two significant transitions as the Weissenberg number is increased. The first is characterized by the onset of a cusp in the stress field centered at the hyperbolic stagnation point in the flow. This cusp becomes more pronounced in time, and our simulations suggest that it is approached exponentially in time. As the Weissenberg number increases further, this cusp "breaks," resulting in unbounded solutions. Again, it appears that the unbounded solutions are approached exponentially in time. Furthermore, for sufficiently large Weissenberg number the rate at which the solution becomes singular decreases in the Weissenberg number.

In these simulations we find that the velocity rapidly approaches a steady-state that remains locally, about the central hyperbolic point, a simple straining flow. This enables us to construct a local solution which agrees remarkably well with our computations. During the preparation of this manuscript we became aware of a construction by Renardy of steady solutions to the UCM model for viscoelastic fluids [9]. This construction is essentially the same as the local solution demonstrated in what follows, though we include time-dependence and study how these singular structures are selected and approached. We also observe that the singularities appear to remain integrable in accordance with finiteness of the systems strain energy.

2 Equations of Motion

We study numerically the two-dimensional Oldroyd-B equations of viscoelastic flow in the low Reynolds number limit. Biperiodic boundary conditions are assumed and persistent curvilinear flows are created by imposing a very simple body force. The Stokes-Oldroyd-B equations are given by:

$$-\nabla p + \triangle \mathbf{u} = -\beta \nabla \cdot \mathbf{S} + \mathbf{f}, \ \& \ \nabla \cdot \mathbf{u} = 0, \tag{1}$$

$$\partial_t \mathbf{S} + \mathbf{u} \cdot \nabla \mathbf{S} - (\nabla \mathbf{u} \mathbf{S} + \mathbf{S} \nabla \mathbf{u}^T) + \tfrac{1}{\mathcal{W}i}(\mathbf{S} - \mathbf{I}) = 0, \tag{2}$$

where $Wi = \tau_p/\tau_f$ is the *Weissenberg number*, with τ_p the polymer relaxation time and τ_f the time-scale of the fluid flow. The dimensional scaling F of the forcing $\mathbf{f}$ is used to set the flow time-scale as $\tau_f = \mu/\rho LF$, where μ is the solvent viscosity, ρ the fluid density, and L the system size. This sets the adimensional force, and the time-scale of transport, to be order one. The parameter $\beta = G\tau_f/\mu$ measures the relative contribution of the polymer stress to momentum balance, where G is the isotropic stress in the polymer field in the absence of flow. Note that Eq. (2) preserves symmetry and positivity of $\mathbf{S}$,

as is expected given its microscopic derivation [8]. The force is given by

$$\mathbf{f} = \begin{pmatrix} -2\sin x \cos y \\ 2\cos x \sin y \end{pmatrix}. \tag{3}$$

In a purely Newtonian Stokes flow ($\beta = 0$) this forcing yields a four vortex "mixer" in each $[0, 2\pi]^2$ cell, like that in Fig.1(a). The solution for the velocity in the Newtonian case is given by

$$\mathbf{u} = \begin{pmatrix} \sin x \cos y \\ -\cos x \sin y \end{pmatrix}. \tag{4}$$

The product of $\beta \cdot \mathcal{W}i = G\tau_p/\mu$ is a material constant, which we set to 1/2. This is consistent with the fluids used in recent experiments of dilute polymer solutions with highly viscous solvents, "Boger fluids" (from [4] the solution viscosity is 1.2 $Pa\ s$, while the solvent (97% glycerol/water) is 0.8 $Pa\ s$, yielding $\beta \cdot \mathcal{W}i = (1.2 - 0.8)/0.8 = 0.5$).

The trace of $\mathbf{S}$ is an important physical quantity representing the amount of stretching of polymer coils. With the constant force given in Eq. (3), and initial data $\mathbf{S}(0) = \mathbf{I}$, many symmetries are maintained in the solution: e.g. $S_{22}(x, y) = S_{11}(y + \pi, x + \pi)$. These symmetries along with the force create a persistent hyperbolic stagnation point in the velocity field. We will refer to the hyperbolic point at (π, π), at which there is extension in the $x-$direction and compression in the $y-$direction, as the *central hyperbolic point.*

The system (1) – (2) has an energy, the "strain energy," given by

$$\mathcal{E} \equiv \int\int \text{tr}\,(\mathbf{S} - \mathbf{I}) dxdy,$$

which satisfies

$$\frac{d}{dt}\mathcal{E} + \frac{1}{\mathcal{W}i}\mathcal{E} = -\frac{2}{\beta}\int\int |\nabla \mathbf{u}|^2 dxdy - \frac{2}{\beta}\int\int \mathbf{u}\cdot\mathbf{f} dxdy. \tag{5}$$

The second term on the right hand side is the power input to the system by the forcing. If it remains bounded, say by C_1, then $\frac{d}{dt}\mathcal{E} + \frac{1}{\mathcal{W}i}\mathcal{E} \leq \frac{2C_1}{\beta}$, which upon intergration yields the bound

$$\mathcal{E}(t) \leq \frac{2C_1\mathcal{W}i}{\beta} + C_2 e^{-t/\mathcal{W}i}. \tag{6}$$

Perhaps surprisingly, Eqs.(1)–(2) are not controlled by diffusion. To see this, consider a linearized version of Eqs.(1) – (2), where

$$\mathbf{f} = \epsilon\mathbf{g},\ \mathbf{u} = \epsilon\mathbf{v},\ \text{ and }\ \mathbf{S} = \mathbf{I} + \epsilon\mathbf{T},$$

for $\epsilon << 1$. The linearized equations are

$$\begin{cases} -\nabla p + \triangle \mathbf{v} = -\beta\nabla\cdot\mathbf{T} + \mathbf{g},\ \ \nabla\cdot\mathbf{v} = 0 \\ \partial_t\mathbf{T} - (\nabla\mathbf{v} + \nabla\mathbf{v}^T) + \frac{1}{\mathcal{W}i}\mathbf{T} = 0. \end{cases} \tag{7}$$

If the Fourier transform is used to solve the linearized equations the evolution of $\hat{\mathbf{T}}$ is given by

$$\partial_t \hat{\mathbf{T}} + \mathbf{L}\left(\frac{k}{|k|}\right)\hat{\mathbf{T}} + \mathbf{P}(k)\hat{\mathbf{g}} = 0, \tag{8}$$

where $\mathbf{L}$ is a linear tensorial operator on the normalized wave vector. Thus, there is no scale-dependent dissipation in the evolution equation for $\mathbf{T}$. This lack of scale-dependent dissipation is one source of difficulties in existence results for these equations (and for numerical difficulties as well). In 2 and 3 dimensions the system has global solutions for small (perturbative) initial data, where the size of the solution depends on the viscosity, however there are no results for global existence if the initial data is large, even for 2D; see [11, 12, 13, 14].

With the constraint $\beta \cdot \mathcal{W}i = C$, one can examine the (formal) limits, $\mathcal{W}i \to 0$, and $\mathcal{W}i \to \infty$. For $\mathcal{W}i << 1$, let

$$\mathbf{u} = \mathcal{W}i\ \mathbf{v} + \text{h.o.t.}, \quad \text{and} \quad \mathbf{S} = \mathbf{I} + \mathcal{W}i\ \mathbf{T} + \text{h.o.t.}.$$

Solving for the leading term in the evolution of $\mathbf{S}$ in Eq. (2) gives

$$\mathbf{T} = \mathcal{W}i(\nabla\mathbf{v} + \nabla\mathbf{v}^T) \Rrightarrow \beta\nabla\cdot\mathbf{T} = C\triangle\mathbf{v}.$$

Hence, in the limit, $\mathbf{v}$ solves the Stokes equation with viscosity $(1 + C)$.

Next consider $\mathcal{W}i >> 1$ and $t \sim \mathcal{O}(1)$. In this formal limit, the equations de-couple, the velocity $\mathbf{v}$ satisfies the Stokes equation with viscosity 1, and the stress satisfies $\mathbf{T} = \mathbf{F}\mathbf{T}(0)\mathbf{F}^T$, where $\mathbf{F}$ is the deformation gradient and satisfies the equation

$$\partial_t\mathbf{F} + \mathbf{v}\cdot\nabla\mathbf{F} = \nabla\mathbf{v}\mathbf{F}.$$

Since $\mathbf{v}$ is steady, this is a linear equation for the deformation gradient. Although both limits $\mathcal{W}i \to 0$ and $\mathcal{W}i \to \infty$ give the Stokes flow for the velocity, there is very interesting (non-Stokesian) behavior for fixed finite $\mathcal{W}i$.

The numerical scheme is a Fourier-based de-aliased spectral method. The stress $\mathbf{S}$ is evolved using a second-order Adams-Bashforth method. Given $\mathbf{S}$, the Stokes equation is easily inverted in Fourier space for $\mathbf{u}$. Given $\mathbf{u}$, the non-linearities of the stress evolution, Eq.(2), are evaluated using $\frac{2}{3}-$rule dealiasing [10]. Care must be taken to maintain good spatial and temporal resolution as the evolving stress field becomes more singular. The spatial discretization is successfully doubled as the active part of the spectrum approaches the Nyquist frequency ($\sim \frac{2}{3}\ N$, where N is the number of physical space points in each direction). Maximal resolutions are 2048^2, and the simulations are stopped before the high wave-number part of the spectrum exceeds 10^{-5}. We find the positive definiteness is maintained in all of our simulations and the time-stepping is verified to have second order accuracy.

3 Numerical Results

First we consider the dynamics for three values of $\mathcal{W}i$ $(0.3, 0.6,$ and $5.0)$ at a fixed time $t = 6$, after evolving from initial data $\mathbf{S} = \mathbf{I}$. These values are chosen

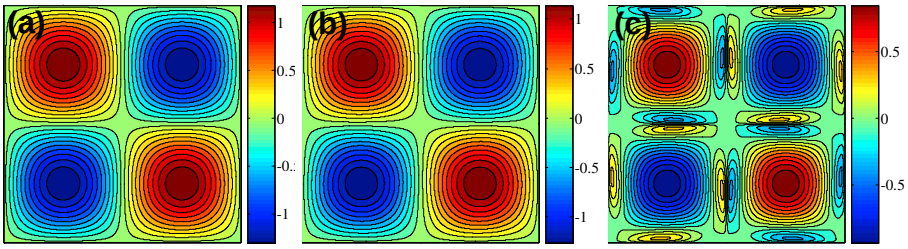

Figure 1: Contour plots of vorticity at $t = 6$: (a) $\mathcal{W}i = 0.3$, (b) $\mathcal{W}i = 0.6$, (c)$\mathcal{W}i = 5$.

to sit between transitions in the solution form as $\mathcal{W}i$ is increased. Figure 1 shows contour plots of the vorticity ω at $t = 6$ for these three values of $\mathcal{W}i$. For the lower Weissenberg numbers the vorticity for the Stokes flow is not changed qualitatively by the addition of the polymer stress, i.e. the four vortex flow persists and no additional features are created. Above a critical Weissenberg number this begins to change, and we see for $\mathcal{W}i = 5$ that additional oppositely signed vortices are generated along the stable and unstable manifolds of the hyperbolic point. Increasing the Weissenberg number decreases the overall magnitude of vortex strength.

Figures 2(a) - (c) show contour plots of tr $\mathbf{S}$ at $t = 6$. At the central hyperbolic point, tr $\mathbf{S}$ is dominated by S_{11}. For $\mathcal{W}i = 0.3$ and 0.6 the solution has essentially relaxed to a bounded steady state by this time. This is not so for $\mathcal{W}i = 5.0$ which appears to be "relaxing" to an unbounded state. The stress field grows rapidly near the hyperbolic points in the flow and concentrates along the unstable manifold of the hyperbolic point; see Fig. 2(c). At this time the solutions remain accurate to within 10^{-8}, which we see by examining the high wave-number part of the spectrum. The shear stress component S_{12} likewise shows transitions in its spatial structure with $\mathcal{W}i$, but remains much smaller in magnitude; see Figs. 2(d) - (f). Figures 2(g) - (i) show contour plots of the first component of the force due to polymer stress at $t = 6$: $F_1 = \partial_x S_{11} + \partial_y S_{12}$ (due to symmetries the second component is a $\pi/2$ rotation of the first). The forces are of much smaller magnitude than the stress components; the large gradients that make up the stress islands in Fig. 2(c) ($\partial_y S_{11}$ and $\partial_x S_{22}$) are not components of the force $\nabla \cdot \mathbf{S}$. It is interesting to note that the only appearance of $\partial_y S_{11}$ ($\partial_x S_{22}$) in Eq. (2) is in the advection term of S_{11} (S_{22}).

Figures 3(a)-(c) show the stress $S_{11}(\pi, y)$ at $t = 6$, i.e. slices along the stable manifold about the hyperbolic point. By this time the stress has begun to concentrate at the central hyperbolic point but for $\mathcal{W}i \lesssim 0.5$ the solutions appear smooth. The first transition appears to occur at $\mathcal{W}i_1 \approx 0.5$ above which the stress remains bounded, but appears to approach a cusp singularity. Above $\mathcal{W}i_2 \approx 0.9$, the maximum of the stress appears to become unbounded in time. We will detail this observation shortly.

Our computations suggest the emergence of a singular algebraic structure of the form $S_{11}(\pi, \pi - y) \sim |y|^q$, near the central hyperbolic point, where q is a function of $\mathcal{W}i$. This is seen from our simulations by analyzing the structure

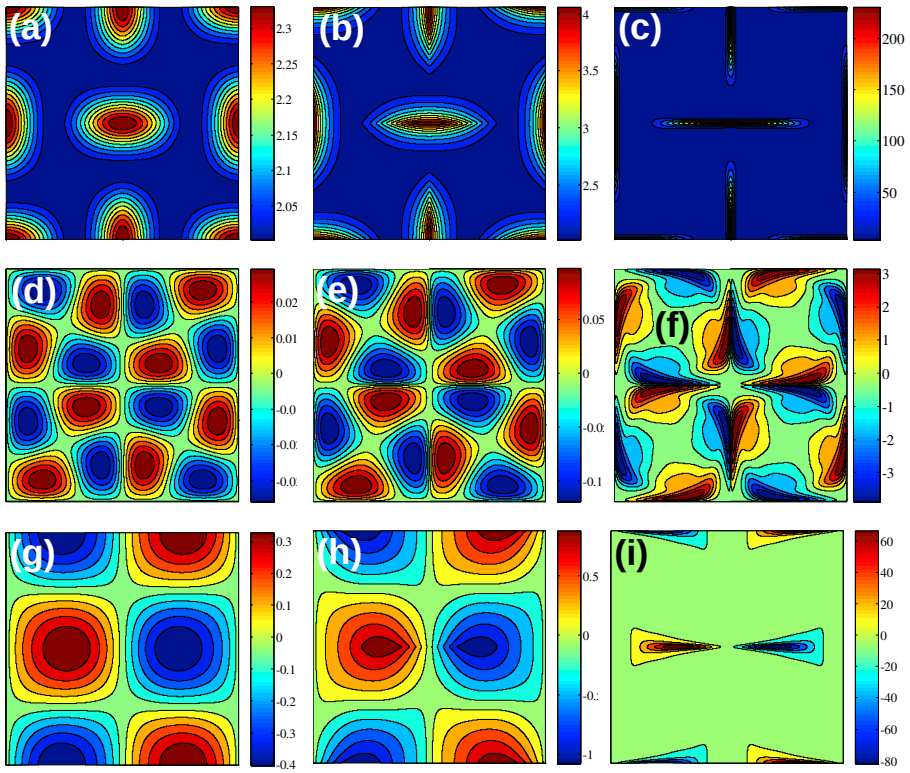

Figure 2: (a) - (c) Contour plots of tr $\mathbf{S}$, for $\mathcal{W}i = 0.3,\ 0.6$, and 5.0, from left to right. S_{11} dominates at the central hyperbolic point, and S_{22} dominates at the hyperbolic point at $(0, \pi)$. (d) - (f) Contour plots of S_{12} for the same values of $\mathcal{W}i$. (g) - (i) Contour plots of the first component of the force due to the polymer stress, $\nabla \cdot (\mathbf{S})_1 = \partial_x S_{11} + \partial_y S_{12}$ for the same values of $\mathcal{W}i$. Note the difference in scale in each case as $\mathcal{W}i$ is increased.

of $\hat{\mathbf{S}}_{11}(\pi, k)$, the Fourier transform (in y) of $S_{11}(\pi, y)$, shown for $\mathcal{W}i = 0.6$ in Fig. 4 (a). In consistency with the emergence of a singular structure, $\hat{\mathbf{S}}_{11}(\pi, k)$ decays less rapidly (in k) as time progresses. To analyze the structure of the singularity we make the Ansatz that $|\hat{\mathbf{S}}_{11}(\pi, k)| \sim Ae^{-\nu k}k^{-p}$, for $|k| >> 1$. This is motivated by Laplace's method for expressing the asymptotic decay of a 1 d Fourier series (for an analytic function) in terms of the distance and algebraic structure of the nearest singularity to the real axis. This method has been used in many numerical studies of singularity formation (e.g. see [15, 16, 17]). The value of ν gives the distance of the singularity to the real axis and p gives its algebraic order. In this Ansatz then, the emergence of the singularity of the form $|y|^q$ is associated with the approach of ν to zero and with $q = p - 1$. $|\hat{\mathbf{S}}_{11}(\pi, k)|$ is fitted to this Ansatz over successive triples of wave number $(k, k+1, k+2)$, yielding pointwise approximations. These fits for $\mathcal{W}i = 0.6$, as an example, are shown in Figs. 4(b) and (c). It is typical that the range in k over which one finds smooth fits in k is limited by attempting to pick out an asymptotic

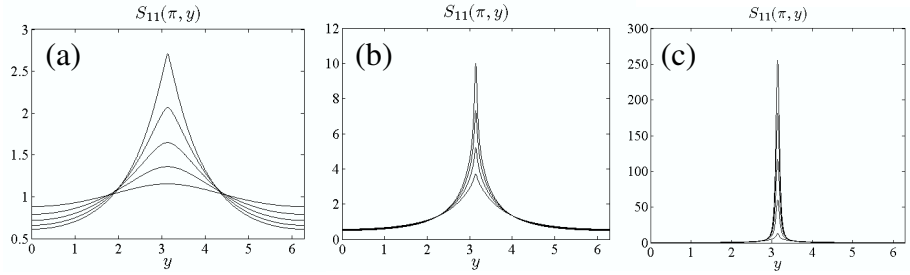

Figure 3: $S_{11}(\pi, y)$, at $t = 6$, increasing in $\mathcal{W}i$. (a) $\mathcal{W}i = 0.1 - 0.5$ (b) $\mathcal{W}i = 0.6 - 0.9$ (c) $\mathcal{W}i = 1 - 5$.

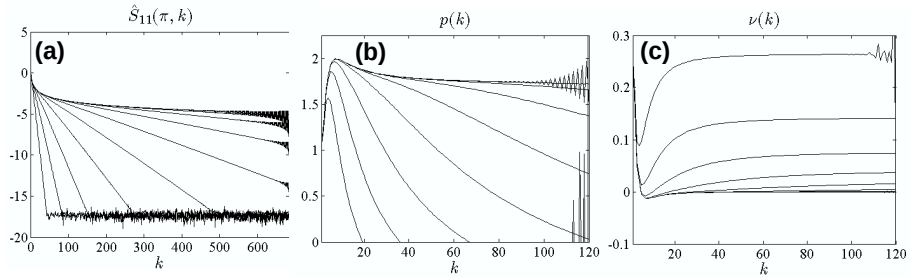

Figure 4: (a) $\hat{\mathbf{S}}_{11}(\pi, k)$ for $\mathcal{W}i = 0.6$ and $t = 1, 2, ..., 10$. The spectrum decays less rapidly as time progresses. (b) For $\mathcal{W}i = 0.6$ and the same times, the fit for the Ansatz $|\hat{S}_{11}(k)| \sim Ae^{-\nu k}k^{-p}$, this computation shows the convergence of p, the algebraic structure of the approached singularity. As time progresses the value $p \approx 1.7$ is approached for a wide value of wave numbers. (c) This computation shows the convergence of ν, the distance from the real axis of the approached singularity. As time progresses the value $\nu = 0$ is approached for a wide value of wave numbers.

decay structure from a solution made increasingly inaccurate by the oncoming singularity (see [17]).

For all Weissenberg numbers our computations suggest $\nu \to 0$ in time, and hence the algebraic structure of the solution becomes progressively more pronounced. The data points in Fig. 5 show the fit exponent, $q = p - 1$, versus the Weissenberg number. We find that q and hence the smoothness of the solution depends sensitively on the Weissenberg number. For $\mathcal{W}i \lesssim \mathcal{W}i_1$ this exponent q is greater than 1, hence the solutions have at least one continuous derivative. The first transition occurs at $q = 1$. Between $\mathcal{W}i_1$ and $\mathcal{W}i_2$, the solutions are cusps; bounded but with a singularity in the first derivative, as $0 < q < 1$. At $\mathcal{W}i = \mathcal{W}i_2$, this singularity becomes unbounded as q becomes negative. Note that the exponent appears to remain bounded below by -1. This would imply that although the stress components are becoming unbounded, they remain integrable. This is supported by Eq. (5), which implies that tr $\mathbf{S}$ remains integrable as long as the input power is bounded. Our computations confirm that the input power does remain bounded as does the strain energy, with the bound given in Eq. (6).

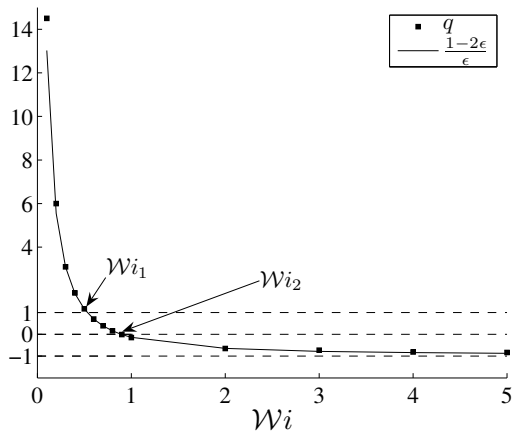

Figure 5: The data points are computed via spectral analysis and plotted for each $\mathcal{W}i$. The solid curve is $\frac{1-2\epsilon}{\epsilon}$, as computed from the local solution of Sect. 4.

We now turn to examining the temporal structure of the stress field. Figs. 6(a) - (f) show slices of the stress S_{11} along both the stable and unstable directions around the hyperbolic point at (π, π) for $t = 1, 2, ..., 10$ for our three example Weissenberg numbers. In the next section we construct a local solution $\tilde{\mathbf{S}}$ about the hyperbolic point. Our simulations and this local solution suggest the form

$$\tilde{S}_{11}(x, y - \pi, t) \approx \bar{S}(\mathcal{W}i) + e^{P(\mathcal{W}i)t} H(ye^{Q(\mathcal{W}i)t}), \tag{9}$$

where $P(\mathcal{W}i) < 0$ for $\mathcal{W}i < \mathcal{W}i_2$, $P(\mathcal{W}i) > 0$ for $\mathcal{W}i > \mathcal{W}i_2$, and $Q(\mathcal{W}i) > 0$. Hence, the exponential rate P controls the rate of convergence (divergence) towards (from) $\bar{S}$, and e^{-Qt} defines a collapsing inner scale of the local solution. To compute P we look at $|S_{11}(\pi, \pi, t) - \bar{S}|$. $\bar{S}(\mathcal{W}i)$ is given in the next section, but the logarithm of this difference is plotted in Fig. 7(a). These curves appear linear (after $t \approx 5$ for $\mathcal{W}i = 5.0$) suggesting an exponential rate. For $\mathcal{W}i < \mathcal{W}i_2$ the peak value, $\bar{S}$, is approached exponentially in time, and for $\mathcal{W}i > \mathcal{W}i_2$ the maximum of the stress is repelled away from $\bar{S}$ exponentially in time. Fig. 7(b) shows this rate, P versus $\mathcal{W}i$. When $\mathcal{W}i > \mathcal{W}i_2$ this approach rate becomes positive and though initially increasing, it eventually ($\mathcal{W}i \gtrsim 2.0$) begins to decrease in $\mathcal{W}i$. Previously we have seen that as $\mathcal{W}i$ is increased the singular solution has an exponent approaching -1 (see Fig. 5) making the solution more difficult to resolve near the hyperbolic point. However, the rate at which the singularity is being approached is decreasing in $\mathcal{W}i$ (past $\mathcal{W}i \gtrsim 2.0$).

To identify the inner-scale, $Q(\mathcal{W}i)$, which is so apparent in Fig.6, we construct the length-scale

$$\lambda(t) = \left(\frac{|S_{11}(\pi, \pi, t) - \bar{S}|}{|\partial_y^2 S_{11}(\pi, \pi, t)|} \right)^{1/2}. \tag{10}$$

λ measures the ratio of the rate at which $S_{11}(\pi, \pi, t)$ approaches (or repels

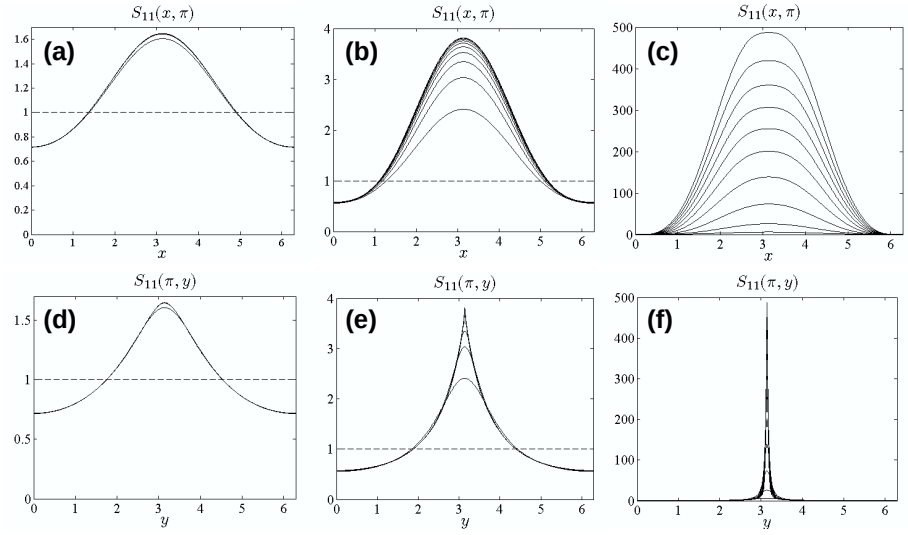

Figure 6: (a) - (c) $S_{11}(x,\pi)$ for $t = 1, 2, ..., 10$, increasing in time for $\mathcal{W}i = 0.3, 0.6$, and 5.0, respectively. (d) - (f) $\mathbf{S}11(\pi, y)$ for $t = 1, 2, ..., 10$, increasing in time for $\mathcal{W}i = 0.3, 0.6$, and 5.0, respectively.

away from) $\bar{S}$, over the rate at which the second derivative is diverging at the central hyperbolic point (at least for $\mathcal{W}i > \mathcal{W}i_1$). This rate is going to zero exponentially fast, as we can see in Fig. 7(c) which shows the logarithm of $\lambda(t)$ for $\mathcal{W}i = 0.3,\ 0.6$ and 5.0. Observe that for $\mathcal{W}i = 0.3 < \mathcal{W}i_1$, this rate appears exponential at first, but after $t \approx 5$ it levels off which suggests that the second derivative is not diverging. This agrees with the fit for the exponent which gives $q \approx 3$, for $\mathcal{W}i = 0.3$. For $\mathcal{W}i > \mathcal{W}i_1$, these curves appear linear (after $t \approx 5$ for $\mathcal{W}i = 5.0$) suggesting an exponential rate. The slope of $\ln(\lambda)$ is the exponential rate of collapse, Q. Figure 7(d) shows Q as a function of the Weissenberg number. The inner scale is collapsing for all $\mathcal{W}i > \mathcal{W}i_1$, and the rate of collapse is decreasing in the Weissenberg number.

4 Comparison with approximate local solution

We can understand many of our computational results in terms of a very simple local model around the hyperbolic point, and hence we examine the local velocity field here. The important observation is that the velocity is approaching steady state for all $\mathcal{W}i$. Figures 8(a) and (b) examine the structure of the local flow about the hyperbolic point for $\mathcal{W}i = 5.0$. At $t = 0$ the velocity is given by the Newtonian solution, given in Eq. (1). For $t > 0$, along the stable and unstable manifolds it appears that $\mathbf{u}_1(x, \pi, t) \approx -\alpha(t)\sin(x)$ and $\mathbf{u}_2(\pi, y, t) \approx \alpha(t)\sin(y)$, for some function $\alpha(t, \mathcal{W}i)$. Computations of the L^2 norms of $\mathbf{u}$ and $\nabla\mathbf{u}$ show that by $t \approx 6$ the norms are reaching a constant value for all $\mathcal{W}i$ considered. Figure 8(c) shows $\alpha(t) = \frac{\partial \mathbf{u}}{\partial x}(\pi, \pi, t)$ as a function of time. We observe that

α decreases in time to an apparently steady value. With this steady value α decreases in Weissenberg number, as seen in Fig. 9(a).

As a simple model we approximate the steady state solution for the velocity near the hyperbolic point by $\mathbf{u} \sim \alpha(-x, y)$, where α is the "large-time" value observed in our simulations. Observe that as $\mathcal{W}i \to 0$, $\alpha \to 2/3$. This is in agreement with the formal limit $\mathcal{W}i \to 0$ discussion from Sect. 2, where $\mathbf{u}$ solves the Stokes equation with viscosity $(1 + C)$, and $C = 1/2$.

To solve for the local structure of $\mathbf{S}$ at a hyperbolic point at the origin we substitute $\mathbf{u} = \alpha(x, -y)$ into the stress advection equation and seek a local solution $\tilde{\mathbf{S}}$. This gives the following PDE for $\gamma = \tilde{S}_{11}$:

$$\partial_t \gamma + \alpha x \gamma_x - \alpha y \gamma_y + (\frac{1}{\mathcal{W}i} - 2\alpha)\gamma - \frac{1}{\mathcal{W}i} = 0.$$

Scaling time as $\mathcal{W}i \cdot t$ and setting $\epsilon = \alpha \mathcal{W}i$ gives

$$\partial_t \gamma + \epsilon x \gamma_x - \epsilon y \gamma_y + (1 - 2\epsilon)\gamma - 1 = 0. \tag{11}$$

This PDE can be solved by the method of characteristics with the general solution given by

$$\gamma(x, y, t) = \frac{1}{(1 - 2\epsilon)} + e^{(2\epsilon-1)t} H_{11}(xe^{-\epsilon t}, ye^{\epsilon t}) \tag{12}$$

for an arbitrary function H_{11}. We seek solutions that yield a time-independent algebraically singular structure in y as $t \to \infty$ and which show little dependence on x. (This latter requirement is already consistent with the dependence of γ upon $xe^{-\epsilon t}$.) Hence for simplicity consider $H_{11}(a, b) \equiv h(b)$ where $h(b) \sim |b|^q$ as $b \to \infty$. One consistent choice would be

$$h(b) = h_0(1 + Cy^2 e^{2\epsilon t})^{q/2}.$$

We determine the exponent q by requiring loss of time dependence of γ for large times, yielding $q = \frac{1-2\epsilon}{\epsilon}$, and large time local solution

$$\gamma_\infty = \frac{1}{1 - 2\epsilon} + A|y|^q. \tag{13}$$

The solution γ_∞ involves a re-scaled time, and also an "effective" Weissenberg number ϵ ("effective" because it scales the actual Weissenberg number by the local rate of strain at the hyperbolic point). Critical values of q occur when $\frac{1-2\epsilon_1}{\epsilon_1} = 1 \Rightarrow \epsilon_1 = 1/3$, and $\frac{1-2\epsilon}{\epsilon} = 0 \Rightarrow \epsilon_2 = 1/2$. If the solution is to remain integrable it must be that $\epsilon < 1$. Figure 9(b) shows the computed value of $\epsilon = \alpha\ \mathcal{W}i$, with the value of α coming from our simulations. The critical values ϵ_1 and ϵ_2 do compare with the critical Weissenberg numbers observed from the computations in Sect. 3, $\mathcal{W}i_1 \approx 0.5$, and $\mathcal{W}i_2 \approx 0.9$. It also appears that $\epsilon < 1$, which implies that the theoretical exponent > -1, and hence the solutions are integrable.

Now we make several other remarks on comparisons with simulations. In Sect. 3 we used the constant $\bar{S} = \frac{1}{1-2\epsilon}$ in the approximation of the exponential rate P. Figure 7(b) compares this rate P with the theoretically predicted exponential rate $\frac{2\epsilon-1}{\mathcal{W}i}$ from Eq. (12). Note that we must divide by $\mathcal{W}i$ because we re-scaled time in Eq. (12). The close comparison of the theoretical exponential rate with the computed exponential rate implies that the particular solution to the PDE (Eq. (13)) is an excellent predictor for the long-time value of $S_{11}(\pi, \pi, t)$, when $\mathcal{W}i < \mathcal{W}i_2$. In fact, for $\mathcal{W}i = 0.1$ the difference is $\mathcal{O}(10^{-14})$.

The exponent $q = \frac{1-2\epsilon}{\epsilon}$ in the local solution γ_∞ from Eq. (13) is compared with the computed exponents (from Sect. 3) in Fig. 5. The comparison is quite good for the range of Weissenberg number.

The general solution to the local problem given in Eq. (12) also predicts an inner scaling form. In the re-scaled variables the inner scaling rate is ϵ, or in the original variables $\frac{\epsilon}{\mathcal{W}i} = \alpha$. Figure 7(d) gives a comparison with the inner scale predicted in Sect. 3, λ. We do not expect the inner scale as defined by λ to have meaning for $\mathcal{W}i < \mathcal{W}i_1$ where the singularities are higher order, and indeed the comparison improves for $\mathcal{W}i > \mathcal{W}i_1$ ($\epsilon \gtrsim .3$), where the second derivative is diverging at the central hyperbolic point.

The approximation $\mathbf{u} = (\alpha x, -\alpha y)$ yields local solutions for the other components of the stress tensor as well. The general solution for S_{22} is given by

$$\tilde{S}_{22}(x, y, t) = \frac{1}{1+2\epsilon} + e^{-(1+2\epsilon)t} H_{22}(xe^{-\epsilon t}, ye^{\epsilon t}).$$

The comparison with the particular solution $\frac{1}{1+2\epsilon}$ is excellent for S_{22}; see Fig. 10(a). $S_{22}(\pi, \pi, t)$ remains bounded for all $\mathcal{W}i$ and the behavior of S_{22} near the central hyperbolic point is less singular than S_{11}. Computing the scaling exponent as was done for S_{11} gives a solution of the form

$$S_{22,\infty} \sim \frac{1}{(1+2\epsilon)} + |y|^{q'}, \tag{14}$$

with $q' = \frac{1}{\epsilon} + 2$. However, when we make the Ansatz $|\hat{\mathbf{S}}_{22}(\pi, k)| \sim Be^{-\mu k} k^{-q'}$, and fit q' it compares well with an exponent of the form $q' = \frac{1}{\epsilon}$, see Fig. 10(b). It is unclear what this discrepency is stemming from. It is possible that the less singular solutions for S_{22} are harder to fit to the Ansatz. Again the distance from the singularity to the real axis, μ, goes to zero for all Weissenberg number, and in fact, $\mu = \nu$, i.e. the singularity for S_{11} is approached at the same rate as the singularity for S_{22}.

The local solution for $\tilde{S}_{12}$ has the form

$$\tilde{S}_{12}(x, y, t) \sim e^{-t} H_{12}(xe^{-\epsilon t}, ye^{\epsilon t}).$$

By symmetry $S_{12} = 0$ around the central hyperbolic point.

The large-time local solutions we construct and those of Renardy in [9] are essentially the same. Renardy considers a steady state problem with a fixed velocity $\mathbf{u} = (x, -y)$. We note that for the dynamic problem constructing the

local solution requires knowledge of the local straining flow at the hyperbolic point (which we compute pointwise from $\nabla \mathbf{u}$ at the central hyperbolic point). Solving for α in general requires matching the inner and outer flow conditions which we have not attempted here. We also observe that theoretically the exponent predicted by Renardy's solution, $1/\mathcal{W}i - 2$, approaches -2, as $\mathcal{W}i \to \infty$. The stress of such a solution would not satisfy the energy law, Eq. (5), as tr $\mathbf{S}$ would not be integrable. We observe in our simulations that $\alpha(\mathcal{W}i)$ decreases in $\mathcal{W}i$ in such a way as to keep tr $\mathbf{S}$ integrable. Knowledge of the local straining flow also gives an "effective" Weissenberg number, ϵ, which gives quite accurate information about the exponential rates of both decay and divergence, the maximum values of the stresses (when bounded) and the inner scaling of the stress field.

5 Other considerations

It is important to note that the observed singularities depend sensitively on many aspects of the problem besides the bare Weissenberg number. For example, we have found that adding a higher order harmonic to the background force will change $\alpha(\mathcal{W}i)$ and hence the order of the singularity. The choice of $\beta \cdot \mathcal{W}i$ also affects α. Our local model is not closed, though it requires only a single number, α, from the simulations. Plainly, there is a matching problem to be solved to self-consistently determine α from the "outer" flow. We have also investigated the robustness of the singularity to dynamical changes in the forcing. For example, we took as initial data a well-resolved but near-cusp solution ($\mathcal{W}i = 0.6$) for a run with $\mathcal{W}i = 0.2$. Fig. 11(a) shows that the solution rapidly relaxes to what appears to be the typical solution for $\mathcal{W}i = 0.2$. The maximum decreases in time and the solution reaches near steady state. Fig. 11(b) shows $\hat{S}_{11}(\pi, k)$. Here the spectrum decays *more rapidly* as time progresses, indicating that the solution is becoming *less* singular in time. Recall that the algebraic structure is approximated as $|y|^q$ where $q = \frac{1-2\epsilon}{\epsilon}$. For $\mathcal{W}i = 0.2$, $q \approx 5.5$, and for $\mathcal{W}i = 0.6$, $q \approx 0.7$. We use the same method as in Sect. 3 to fit the exponent with this data and $p(k)$ is plotted in Fig. 11(c). Initially the fit gives $p(k) \sim 1.7$ which indicates a cusp. As time progresses the fit appears to give $p \sim 1.7$ for lower wave numbers and $p \sim 6.7$ for higher wave numbers. By $t = 10$, the fit appears to give $p \sim 6.7$ for all wave numbers (where convergence is seen). This seems to suggest that initially the more dominant singularity has $p = 1.7$ which agrees well with $\mathcal{W}i = 0.6$, and then as time progresses this singularity diminishes and the singularity with $p = 6.7$, corresponding to $\mathcal{W}i = 0.2$, becomes more dominant.

The Oldroyd-B equations are often criticized for allowing infinite extensibility of polymer chains. Indeed, those singular solutions with $\mathcal{W}i > \mathcal{W}i_2$ correspond to arbitrarily large extension. Still, we have also found a whole spectrum of solutions with finite extension which are singular nonetheless. To understand whether the singularities we have observed are due to this infinite extensibility we add a FENE-P cutoff to our model [18]. The Stokes-Oldroyd-B equations

with the FENE-P penalization are given by:

$$-\nabla p + \triangle \mathbf{u} = -\beta \nabla \cdot \mathbf{S} + \mathbf{f}, \ \& \ \nabla \cdot \mathbf{u} = 0,$$
$$\partial_t \mathbf{C} + \mathbf{u} \cdot \nabla \mathbf{C} - (\nabla \mathbf{u} \mathbf{C} + \mathbf{C} \nabla \mathbf{u}^T) + \tfrac{1}{\mathcal{W}i}(\mathbf{S} - \mathbf{I}) = 0,$$
$$\mathbf{S} = \tfrac{\mathbf{C}}{1 - (\frac{\mathrm{tr}\, \mathbf{C}}{\ell^2})},$$

where ℓ represents the ratio of the maximum polymer length to the length of the polymer when coiled. In what follows we use $\ell = 10$. We consider two cases, $\mathcal{W}i_1 < \mathcal{W}i < \mathcal{W}i_2$, and $\mathcal{W}i > \mathcal{W}i_2$.

In the first case we consider $\mathcal{W}i = 0.6$. Fig. 12(a) shows slices of $S_{11}(\pi, y)$ for $t = 0, 1, ..., 10$. The solution appears to be approaching a cusp singularity quite similar to $\mathcal{W}i = 0.6$ without the FENE-P penalization; see Fig. 6(e). Fig. 12(b) shows the value of tr $\mathbf{S}(\pi, \pi, t)$ for $\mathcal{W}i = 0.6$ both with and without the FENE-P penalization. We see that the penalization reduces the maximum value of the stress, but in this range of $\mathcal{W}i$, the maximum value is bounded even without the penalization and the differences are minimal. Fits of Fourier spectrum for the algebraic order give a cusp singularity similar to the case without the FENE-P penalization. In summary, the FENE-P penalization does not smooth out the cusp and hence any difficulties in numerical simulations related to the large gradients in the stress field at the central hyperbolic point will still be apparent.

For $\mathcal{W}i > \mathcal{W}i_2$, the FENE-P penalization does appear to keep tr $\mathbf{S}$ bounded. For $\mathcal{W}i = 2.0$, Fig. 12(c) shows slices of $S_{11}(\pi, y)$ for $t = 0, 1, ..., 10$, and Fig. 12(d) shows tr $\mathbf{S}(\pi, \pi, t)$ for $\mathcal{W}i = 0.6$ with and without the FENE-P penalization. It appears that tr $\mathbf{S}$ is bounded (perhaps asymptotically by 100) with the FENE-P penalization. The fit of the Fourier spectrum in this case gives evidence of an oncoming singularity but the results appear to indicate that the solution should be approaching an unbounded solution. This may be due to problems with the method of fitting the exponent in this case, or perhaps the Ansatz is inappropriate. In any event the solution appears to remain bounded and appears to approach a cusp singularity. Although these results are not conclusive it does appear that at least a simple FENE-P penalization will not resolve all of the difficulties associated with the Oldroyd-B equations, and that allowing infinite extensibility in polymer chain lengths is not at the root of all the difficulties with these equations. We suspect that FENE may suffer from similar difficulties.

6 Conclusion

The behavior and smoothness of solutions to the Stokes-Oldroyd-B equations is very sensitive to the Weissenberg number. Nearly singular structures in the stress field arise at every Weissenberg number. We observe two dramatic transitions which for our simulations occur for $\mathcal{W}i_1 \approx 0.5$ and $\mathcal{W}i_2 \approx 0.9$. The first, at $\mathcal{W}i_1 \approx 0.5$, is distinguished by the appearance of a cusp singularity in the stress field which is approached exponentially in time at the central hyperbolic point in the flow. Below this critical Weissenberg number, although one or more

derivatives of the stress may be bounded, the solutions are still approaching a singular solution. At higher Weissenberg number (beyond $\mathcal{W}i_2 \approx 0.9$) the singular structures that are approached are unbounded at the central hyperbolic point.

The constructed local solution agrees quite well with the numerical results giving similar dependence on $\mathcal{W}i$ for regularity of solutions, exponential rate, and inner scaling. The constructed local solution also introduces the new parameter ϵ, the "effective" Weissenberg number. The nature of the singularity depends critically on ϵ which includes of course the Weissenberg number, but also the local strain rate of the flow at the hyperbolic point, α. Currently we approximate α with our simulations, however it should be possible to solve for α in general by matching the inner and outer flow conditions. This is a complicated problem but well worth studying.

An interesting point to reiterate is the fact that although there is significant evidence that for $\mathcal{W}i > \mathcal{W}i_1$ first derivatives of the stress are growing exponentially fast, these very large derivatives are not components of the polymer stress, and hence do not directly feed back into the Stokes equation. One might be able to use this fact to obtain bounds on the stress which in turn yield bounds on $\mathbf{u}$ to show that the solutions (although exponentially large) remain bounded for all time.

It may be these potential infinite time singularities which are at the root of the difficulties in numerical simulations of viscoelastic fluids using the Oldroyd-B model. There is a vast literature regarding the "high Weissenberg" number problem; see [19], Chapter 7, for a careful exposition of many relevant results. It appears that the solution to the Oldroyd-B equations in any flow which contains a hyperbolic stagnation point will develop large stress gradients at an exponential rate, even for Weissenberg number much lower than those which are related to the infinite extension of polymer chains. These large stress gradients (due to the cusp singularity) will be present even with a restriction on the length of the polymer chains. We have added a simple FENE-P penalization to our numerical simulation and observe that for $\mathcal{W}i < \mathcal{W}i_2$ there is still an exponential approach to a cusp singularity, and for $\mathcal{W}i > \mathcal{W}i_2$ although tr $\mathbf{S}$ is bounded, there remains an approach to a cusp singularity. We believe that the real difficulties stem from the lack of scale dependent dissipation in the stress advection.

The authors would like to thank Estarose Wolfson at the Courant Institute for porting our spectral code to the NYU MAX cluster. In addition we would like to thank NYU for the use of the MAX cluster. The first author was partially supported by NSF grant DMS-0600668. The second author was partially supported by a grant from the DOE.

References

[1] A. Groisman and V. Steinberg. Elastic turbulence in a polymer solution flow. *Nature*, 405:53–55, 2000.

[2] A. Groisman and V. Steinberg. Efficient mixing at low reynolds numbers using polymer additives. *Nature*, 410:905–908, 2001.

[3] A. Groisman and V. Steinberg. Elastic turbulence in curvilinear flows of polymer solutions. *New Journal of Physics*, 4:74437–7, 2004.

[4] P.E. Arratia, C.C. Thomas, J. Diorio, and J.P. Gollub. Elastic instabilities of polymer solutions in cross-channel flow. *Phys. Rev. Letters*, 96:144502, 2006.

[5] B. Thomases and M. Shelley. Coil-stretch transitions and mixing in a viscoelastic fluid. *In Preparation.*

[6] J. M. Rallison and E. J. Hinch. Do we understand the physics in the constitutive equation? *J. of Non-Newt Fluid Mech.*, 29:37–55, 1988.

[7] R. B. Bird, O. Hassager, R.C. Armstrong, and C.F. Curtiss. *Dynamics of Polymeric Liquids, Vol. 2: Kinetic Theory.* John Wiley and Sons, 1980.

[8] R.G. Larson. *The Structure and Rheology of Complex Fluids.* Oxford University Press, 1998.

[9] M. Renardy. A comment on smoothness of viscoelasitc stresses. *J. of Non-Newt Fluid Mech.*, 138:204–205, 2006.

[10] Roger Peyret. *Spectral Methods for Incompressible Viscous Flow.* Springer, New York, 2002.

[11] F. H. Lin, C. Liu, and P. Zhang. On hydrodynamics of viscoelastic fluids. *Comm. Pure Appl. Math.*, 58.

[12] T. C. Sideris and B. Thomases. Global existence for three-dimensional incompressible isotropic elastodynamics via the incompressible limit. *Comm. Pure Appl. Math.*, 58.

[13] P. L. Lions and N. Masmoudi. Global solutions for some oldroyd models of non-newtonian flows. *Chinese Ann. Math. Ser. B*, 21:131–146, 2000.

[14] J.Y. Chemin and N. Masmoudi. About lifespan of regular solutions of equations related to viscoelastic fluids. *SIAM J. Math. Anal.*, 33:84–112, 2001.

[15] P. L. Sulem C. Sulem and H. Frisch. Tracing complex singularities with spectral methods. *J. Comput. Phys.*, 50:138–161, 1981.

[16] R. Krasny. A study of singularity formation in a vortex sheet by the point-vortex approximation. *J. Fluid Mech.*, 167:65–93, 1986.

[17] M. J. Shelley. A study of singularity formation in vortex-sheet motion by a spectrally accurate vortex method. *J. Fluid Mech.*, 242:493–526, 1992.

[18] R.B. Bird, P.J. Dotson, and N.L. Johnson. Polymer solution rheology based on a finitely extensible bead-spring chain model. *J. of Non-Newt Fluid Mech.*, 7:213–235, 1980.

[19] R.G. Owens and T.N. Phillips. *Computational Rheology*. Imperial College Press, 2002.

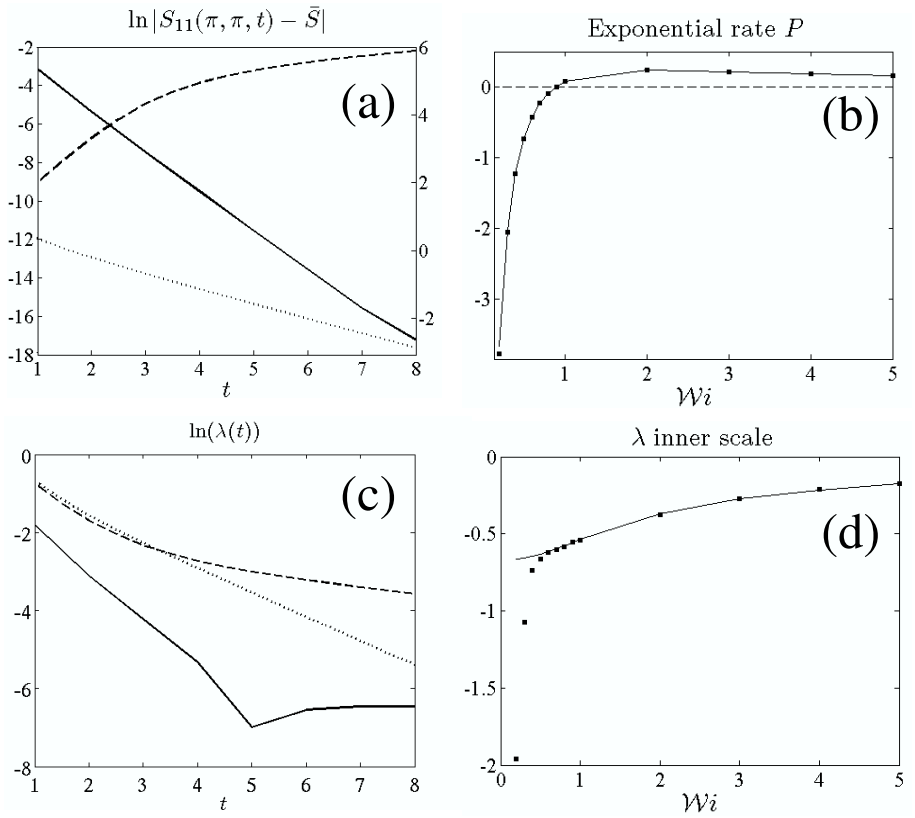

Figure 7: (a) $\ln(|S_{11}(\pi,\pi,t)-\bar{S}|)$ for $\mathcal{W}i = 0.3$, (solid curve with scale on left axis) $\mathcal{W}i = 0.6$, (dotted curve with scale on right axis) and $\mathcal{W}i = 5.0$, (dashed curve with scale on right axis). The curves are approximately linear after some time giving an exponential rate of convergence towards (negative slope) or divergence from (positive slope) $\bar{S}$ for $\mathbf{S}11(\pi,\pi,t)$. The slope for each $\mathcal{W}i$ gives the exponential rate $P(\mathcal{W}i)$. (b) The exponential rate P is plotted versus Weissenberg number. Curve is $\frac{2\epsilon-1}{\mathcal{W}i}$, as computed from the local solution of Sect. 4. (c) $\ln(\lambda(t))$ for each value $\mathcal{W}i = 0.3$, (solid curve) $\mathcal{W}i = 0.6$, (dotted curve) and $\mathcal{W}i = 5.0$, (dashed curve). $\mathcal{W}i = 0.3 < \mathcal{W}i_1$ the second derivative at the hyperbolic point is not diverging and the curve levels off as the peak value is approached. For $\mathcal{W}i > \mathcal{W}i_1$ the curves are approximately linear after some time, indicating an exponentially collapsing inner scale. The slope for each $\mathcal{W}i$ gives the collapse rate $Q(\mathcal{W}i)$. (d) The inner scale Q is plotted versus the Weissenberg number. The solid curve is $\frac{-\epsilon}{\mathcal{W}i}$, as computed from the local solution of Sect. 4.

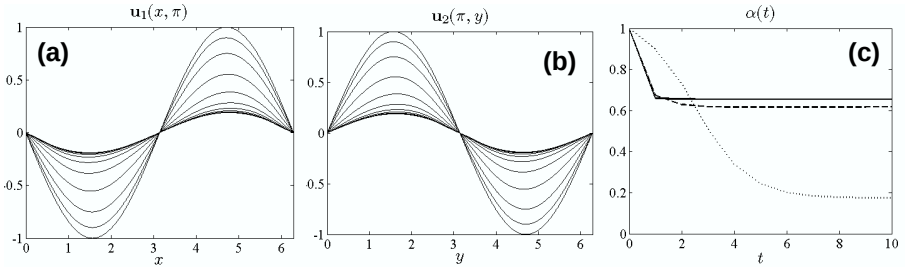

Figure 8: (a) Velocity $\mathbf{u}_1(x,\pi,t)$ for $\mathcal{W}i = 5.0$, for $t = 0, 1, ..., 10$. The initial data, $\mathbf{u}_1(x,\pi,0) = -\sin x$ and $\mathbf{u}_1$ decreases in time (from $t = 0$ to $t = 10$) to a steady solution. (b) $u_2(\pi,y,t)$ for $t = 1, 2, ..., 10$ decreasing to a steady solution. (c) The strain rate at the central hyperbolic point, $\alpha(t) = \frac{\partial \mathbf{u}}{\partial x}(\pi,\pi,t)$ for $\mathcal{W}i = 0.3$ (solid), 0.6, (dashed) and 5.0, (dotted).

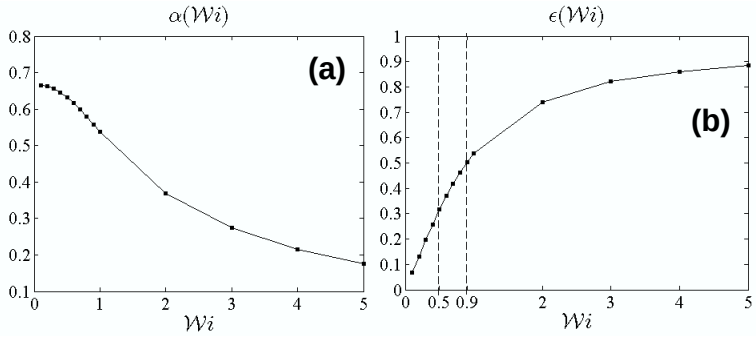

Figure 9: (a) The converged strain rate $\alpha = \frac{\partial \mathbf{u}}{\partial x}(\pi,\pi)$ at the central hyperbolic point. α at steady state decreases as a function of $\mathcal{W}i$ (b) "Effective" Weissenberg number $\epsilon = \alpha\ \mathcal{W}i$ is plotted as a function of $\mathcal{W}i$, from computed values of α, $\epsilon_1 = 1/3$ corresponds to $\mathcal{W}i_1 \approx 0.5$ and $\epsilon_2 = 1/2$ corresponds to $\mathcal{W}i_2 \approx 0.9$.

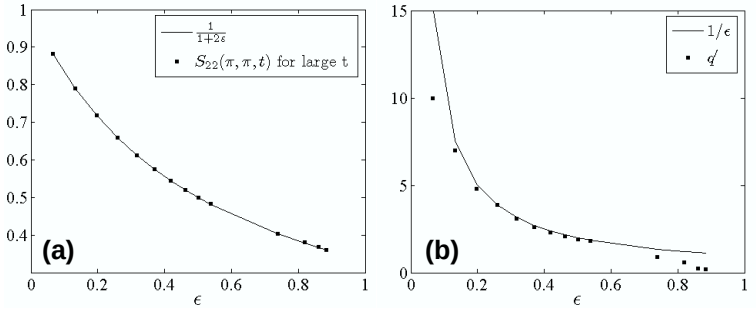

Figure 10: (a) For S_{22} : a comparison of the constant term of the local solution, $\bar{S}_{22} = \frac{1}{1+2\epsilon}$, with the "large time" of converged value of $S_{22}(\pi,\pi,t)$. (b) For S_{22} : a comparison of a possible scaling exponent, $\frac{1}{\epsilon}$, with the exponent, q, estimated from the Fourier spectra.

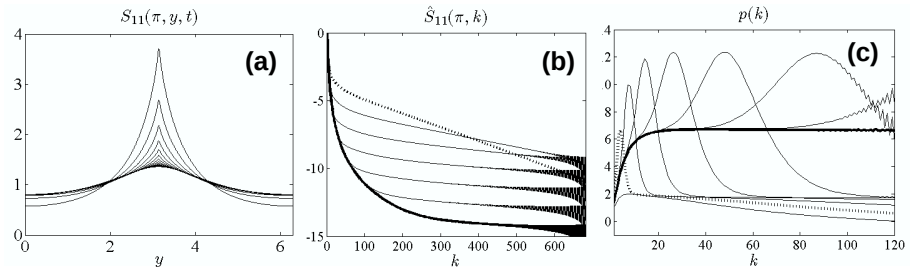

Figure 11: (a) Stress $S_{11}(\pi, y)$ for $t = 0, 1, ..., 10$ decreasing in time. Initial data comes from cusp solutions with $\mathcal{W}i = 0.6$ which is changed to $\mathcal{W}i = 0.2$ immediately. (b) Plot of $\hat{S}_{11}(\pi, k)$, the Fourier spectrum decays more rapidly in time indicating that the singularity may be changing. The dotted line is for $t = 0$ and the solid line is for $t = 10$. (c) Plot of fit to compute algebraic order of singularity, $|y|^q$, with $q = p - 1$. Time progresses from the heavy dotted line to the heavy solid line. Initially the fit $p \sim 1.7$ (indicating a cusp) is dominant but as time progresses the line $p \sim 6.5$, is dominant (indicating an increase in smoothness of the solution).

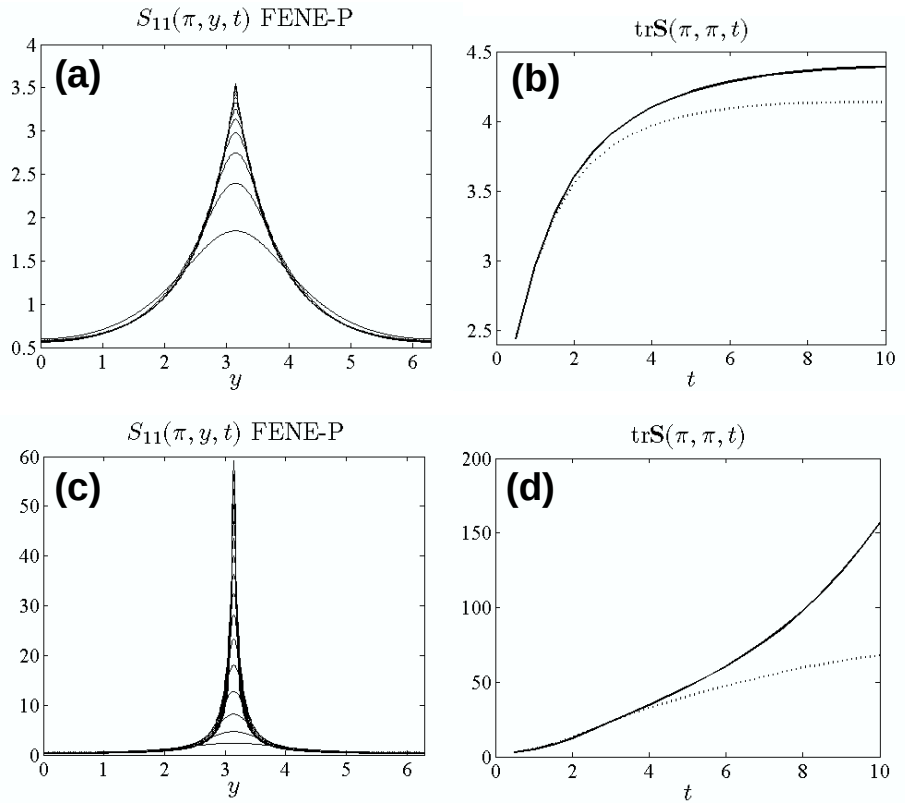

Figure 12: (a) Plots of $S_{11}(\pi, y, t)$, with FENE-P penalization, increasing in time to cusp-like solution, $\mathcal{W}i = 0.6$. (b) Comparison of tr $\mathbf{S}(\pi, \pi, t)$ with FENE-P penalization (dotted line) and without the FENE-P penalization (solid line), $\mathcal{W}i = 0.6$. (c) Plots of $S_{11}(\pi, y, t)$, with FENE-P penalization, increasing in time to cusp-like solution, $\mathcal{W}i = 2.0$. (d) Comparison of tr $\mathbf{S}(\pi, \pi, t)$ with FENE-P penalization (dotted line) and without FENE-P penalization (solid line), $\mathcal{W}i = 2.0$.